machines

MDPI

Article

Influence of Wideband Cable Model for Electric Vehicle Inverter–Motor Connections: A Comparative Analysis

Easir Arafat and Mona Ghassemi *

Zero Emission, Realization of Optimized Energy Systems (ZEROES) Laboratory, Department of Electrical and Computer Engineering, The University of Texas at Dallas, Richardson, TX 75080, USA; easir.arafat@utdallas.edu
* Correspondence: mona.ghassemi@utdallas.edu

Abstract: Electric vehicles (EVs) rely on robust inverter-to-motor connections to ensure high-efficiency operation under the challenging conditions imposed by wide-bandgap (WBG) semiconductors. High switching frequencies and steep voltage rise times in WBG inverters lead to repetitive transient overvoltages, causing insulation degradation and premature motor winding failure. This study proposes a wideband (WB) model of EV cables, developed in EMTP-RV, to improve transient voltage prediction accuracy compared to the traditional constant parameter (CP) model. Using a commercially available EV-dedicated cable, the WB model incorporates frequency-dependent parasitic effects calculated through the vector fitting technique. The motor design is supported by COMSOL Multiphysics and MATLAB 2023 simulations, leveraging the multi-conductor transmission line (MCTL) model for validation. Using practical data from the Toyota Prius 2010 model, including cable length, motor specifications, and power ratings, transient overvoltages generated by high-frequency inverters are studied. The proposed model demonstrates improved alignment with real-world scenarios, providing valuable insights into optimizing insulation systems for EV applications.

Keywords: wideband cable modeling; EV; wide-bandgap (WBG) inverters; MCTL theory; CP model; finite element analysis (FEM); vector fitting algorithm; transient overvoltages

check for updates

Academic Editor: Antonio J. Marques Cardoso

Received: 26 January 2025
Revised: 22 February 2025
Accepted: 24 February 2025
Published: 27 February 2025

Citation: Arafat, E.; Ghassemi, M. Influence of Wideband Cable Model for Electric Vehicle Inverter–Motor Connections: A Comparative Analysis. *Machines* **2025**, *13*, 189. https://doi.org/10.3390/machines13030189

Copyright: © 2025 by the authors. Licensee MDPI, Basel, Switzerland. This article is an open access article distributed under the terms and conditions of the Creative Commons Attribution (CC BY) license (https://creativecommons.org/licenses/by/4.0/).

1. Introduction

The rapid growth of EV has catalyzed advancements in inverter technology, enabling higher efficiency, power density, and reliability in drivetrain systems [1,2]. The advent of WBG semiconductors, such as Silicon Carbide (SiC) and Gallium Nitride (GaN), and their extension into ultra-wide-bandgap (UWBG) devices has further revolutionized power electronics by enabling inverters to operate at significantly higher switching frequencies and with faster voltage rise times than conventional silicon-based devices [3,4]. These innovations allow for compact designs, reduced losses, and improved thermal management, making them ideal for EV applications [5]. For instance, inverters employing WBG devices can achieve switching frequencies in hundreds of kilohertz, ensuring high power efficiency for demanding applications such as the Toyota Prius and Tesla Model S.

Despite these benefits, WBG-based inverters introduce new challenges, particularly for the insulation systems within motor windings and terminals. High-frequency switching and rapid voltage transitions generate repetitive transient overvoltages, placing considerable stress on insulation materials. Over time, these stresses can cause localized heating, partial discharges, and insulation degradation, potentially leading to dielectric breakdown [6–9]. Real-world failures in industrial motors and traction systems underscore the urgent need to analyze and mitigate transient voltage effects in EV drivetrains.

To address these challenges, accurate system modeling—including the inverter-to-motor cable and motor windings—is essential. Frequency-dependent parameters and the rapid voltage transitions inherent to WBG-based inverters influence the transient effects in these components. Traditional models, such as the CP model, assume static electrical properties and fail to capture frequency-dependent behaviors, such as skin and proximity effects, which become significant at high frequencies. The frequency-dependent (FD) model improves accuracy by incorporating these effects but is computationally intensive [10]. A more advanced alternative, the WB model, is implemented in electromagnetic transient programs like EMTP-RV [11]. This model accounts for frequency-dependent resistances, capacitances, and inductances, providing a more precise representation of high-frequency behaviors in WBG-driven systems.

When modeling motor windings, transient overvoltage effects must be carefully considered. MCTL theory provides a robust framework for modeling parasitic elements within motor windings, including turn-to-turn capacitance, turn-to-ground capacitance, self-inductance, mutual inductance, and resistance [12–14]. These parameters are typically derived using finite element analysis (FEA) tools such as COMSOL Multiphysics, which apply electrostatic and magnetic solvers to capture frequency-dependent effects [15,16]. Studies leveraging MCTL-based modeling have demonstrated its ability to accurately predict transient overvoltages, particularly in inverter-fed motor windings operating at high switching frequencies [15].

Some authors provide a detailed analysis of cable modeling techniques, including lumped and distributed models, and emphasize the importance of considering frequency-dependent parameters such as inductance, resistance, and capacitance for accurately capturing high-frequency behavior in cables [17]. These models allow for a better simulation of cable impedance, reflection voltages, and the overall interaction between the cable and the motor winding. On the other hand, some focused on modeling the conductor and cable connections to the motor, proposing a universal gray-box model for a permanent magnet synchronous machine (PMSM) [18,19]. This model includes frequency-dependent mutual impedance between the various conductors and capacitive and inductive coupling between turns and the winding housing. The authors validated their model using impedance measurements, showing a low error margin (6.5%) between simulated and measured voltage distributions at various switching frequencies. This modeling approach for the connected conductor allows for a better prediction of voltage stress along the cables and improves the overall accuracy when combined with the motor winding model.

Regarding cable modeling, while FEA or MCTL-based methods can be employed, using EMTP-RV for cable simulation offers a significantly faster modeling process, making it a practical choice for large-scale simulations, which is absent in previous studies. The CP model, while computationally simple, lacks accuracy at high frequencies, and the FD model, though more precise, is computationally demanding. The WB model balances accuracy and efficiency, making it the preferred approach for cable simulation in this study, which is the main focus of the study.

To validate this integrated modeling approach, real-world data from the Toyota Prius 2010 model are used [20]. These data help to ensure that the simulation results accurately reflect the voltage behavior in practical systems, particularly under varying switching conditions. Using an EMTP-RV-based model for the cable and an FEM-based model for the motor windings, this study creates a comprehensive framework that captures both high-frequency dynamics and transient overvoltage effects, ensuring a reliable prediction of insulation system performance in WBG-based drive systems.

2. Methodology

This study focuses on modeling the transient overvoltages generated at the motor terminals of an EV drivetrain due to impedance mismatches between the cable and motor windings, a phenomenon exacerbated by UWBG inverters. These inverters operate at high switching frequencies and steep voltage rise times, causing significant reflections and non-uniform voltage distributions at the motor terminals, which can easily be described with the phenomenon of the traveling waves on a line [21,22]. The mismatch between the surge impedance of the cable (Z_c) and the motor (Z_m) leads to wave reflections governed by the reflection coefficient presented in Equation (1):

$$r = \frac{Z_m - Z_c}{Z_m + Z_c} \tag{1}$$

where r in Equation (1) represents the fraction of the incident wave reflected at the motor terminals. When $Z_m \gg Z_c$, the reflected voltage approaches the incident voltage in magnitude, resulting in overvoltage scenarios that stress the insulation system. This transient behavior highlights the necessity of precise modeling to ensure system reliability. The WB model needs to be employed for the cable to address this issue adequately. At the same time, the MCTL theory needs to be utilized to model the motor windings, enabling high-fidelity simulation of these transient phenomena [15].

In this case, the Toyota Prius 2010 model is the benchmark for validating simulations with real-world conditions. Practical data from this vehicle is incorporated into the models. The Toyota Prius 2010's power control unit (PCU) provides a practical framework for the analysis [21], demonstrated in Figure 1. It integrates the inverter, cable, and motor into a unified system, ensuring that transient voltage effects, such as those caused by wave reflections due to impedance mismatches, are evaluated under realistic operating conditions. By leveraging this setup and accurately capturing reflected wave phenomena, the study bridges theoretical modeling and real-world validation, providing critical insights into mitigating transient overvoltages and optimizing insulation design for high-frequency UWBG inverter-driven systems.

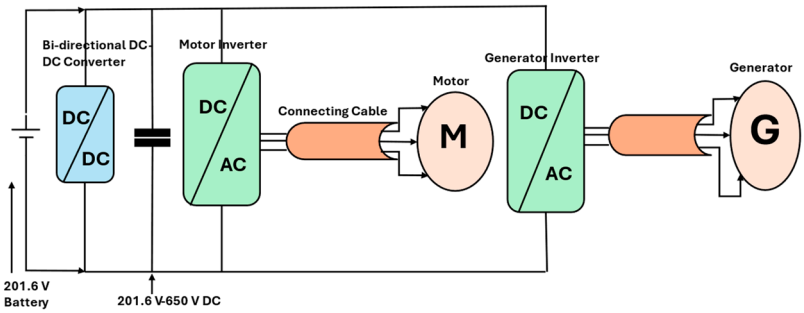

Figure 1. Circuit diagram of 2010 Prius power control unit [20].

The Toyota Prius 2010 PCU exemplifies advanced integration and thermal management, featuring a lightweight aluminum cooling infrastructure and a compact design. The PCU consolidates key components such as the bi-directional DC-DC converter, motor inverter, and generator inverter onto two PCBs, enhancing efficiency and reducing weight to 13.0 kg. Powered by a 201.6 V battery, the PCU boosts the voltage to 202–650 V based on driving conditions, employing a network of high-performance capacitors for filtering and stability. This design streamlines the power system and ensures effective heat dissipation, making it an ideal benchmark for analyzing transient overvoltages in EV drivetrains.

In addition to voltage boosting and power conversion, the PCU plays a role in the vehicle's grounding strategy. The high-voltage system in the Prius follows an isolated

ground configuration, where the PCU, battery, and motor operate on a floating ground, minimizing leakage currents and reducing the risk of ground loops that could increase chaos in transient overvoltages. However, control electronics and low-voltage accessories are typically referenced to chassis ground, ensuring proper EMI shielding. The effectiveness of this hybrid grounding configuration is particularly important in mitigating transient voltage buildup when switching events occur in the inverter.

2.1. Cable Modeling

The representation of insulated cables for electromagnetic transient simulations in EMTP-type programs requires detailed modeling of cable parameters derived from geometrical configurations and material properties [23]. WB modeling enables the calculation of series impedance and shunt admittance matrices, which capture the frequency-dependent effects of resistance, inductance, and capacitance. Unlike constant parameter (CP) models, WB models incorporate the skin effect and parasitic elements across a wide frequency range, providing realistic results for high-frequency transient phenomena [11].

The CP model assumes a single-frequency calculation of per-unit-length parameters, leading to inaccuracies in transient analysis. The transmission line equations are given by [11,21,22]

$$\frac{\partial V(x,s)}{\partial x} = -Z'I(x,s) \tag{2}$$

$$\frac{\partial I(x,s)}{\partial x} = -Y'V(x,s) \tag{3}$$

where the per-unit-length impedance and admittance in the CP model are expressed as follows:

$$Z' = R' + sL' \tag{4}$$

$$Y' = G' + sC' \tag{5}$$

In the CP model, the values of R' and Y' are assumed constant, ignoring their frequency dependence. This simplification fails to account for frequency-dependent phenomena such as the skin and proximity effects, which significantly impact transient voltage waveforms.

The WB model overcomes these limitations by using rational function approximations to represent the complete frequency-dependent behavior. The series impedance, considering the skin effect, is given by

$$Z'(\omega) = R(\omega) + j\omega L(\omega) \tag{6}$$

where the AC resistance $R(\omega)$ is frequency-dependent due to the skin effect:

$$R(\omega) = \frac{1}{2\pi\sigma\delta}\left(1 + \frac{\delta}{r}\right) \tag{7}$$

with δ given by

$$\delta = \sqrt{\frac{2}{\mu\sigma\omega}} \tag{8}$$

where μ is the magnetic permeability, σ is the conductivity, and ω is the angular frequency.

Similarly, the proximity effect, which results in uneven current distribution due to mutual coupling in adjacent conductors, is accurately modeled in the WB framework. The effective impedance with proximity effect is as follows:

$$Z'_{prox}(\omega) = Z'_{self}(\omega) + Z'_{mutual}(\omega) \tag{9}$$

where

$$Z'_{mutual}(\omega) = \frac{\mu\omega}{2\pi}\ln\left(\frac{D}{r}\right) \tag{10}$$

where D is the center-to-center distance between adjacent conductors.

Moreover, the WB model approximates frequency-dependent parameters using vector fitting:

$$Y_c(s) \approx G_0 + \sum_{i=1}^{N_y} \frac{G_i}{s - q_i} \tag{11}$$

$$H(s) \approx \sum_{i=1}^{M_i} \sum_{k=1}^{M_i} \frac{R_{i,k}}{s - p_{i,k}} e^{-sT_i} \tag{12}$$

where G_0 is a constant matrix, and q_i, $p_{i,k}$ are fitting poles. This approach allows the WB model to accurately represent transient waveforms, ensuring realistic simulations of fast-rising pulses encountered in wide-bandgap inverter applications.

While typical Cable Constant routines simplify parameter calculation by assuming frequency-independent permittivity and neglecting skin and proximity effects (like the CP model), WB modeling overcomes these limitations by accurately representing the dynamic behavior of real-world cable designs in modern EMTP software (version 4.4.0) [23]. This approach can consider the impact of stranded conductors, semiconducting screens, and protective jackets, enabling precise simulation of electromagnetic transients and voltage reflections in EV cables.

For this study, the RADOX Elastomer S (FHLR4GC13X) cable, manufactured by HUBER+SUHNER (Charlotte, NC, USA), was selected for modeling using the WB model. This cable is specifically designed for high-voltage automotive applications, with a voltage rating of 1 kV AC and 1.5 kV DC and an operating temperature range of −40 °C to 150 °C [24]. A 36-inch cable connected the voltage source to the motor in our setup. Structurally, this cable features a multilayer coaxial design, incorporating a stranded bare copper conductor, an insulation layer of RADOX 155, a tinned copper screen for electromagnetic shielding, and an outer sheath made of RADOX Elastomer S for mechanical and environmental protection. Additionally, the cable includes two thin tape layers—one between the conductor and the RADOX 155 insulation and another between the screen and the RADOX Elastomer S sheath. However, these tape layers were omitted during simulation due to their negligible thickness, simplifying the EMTP modeling process without significantly affecting accuracy. The complete cable construction is illustrated in Figure 2.

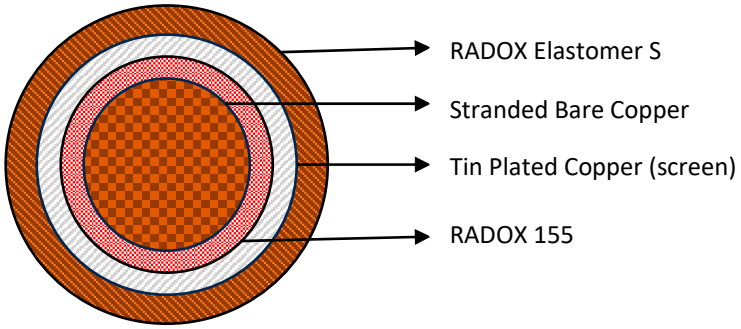

Figure 2. Construction of the cable [24].

We modeled a single-core (SC) cable in EMTP, positioned 6 inches above the ground to approximate the Toyota Prius 2010's ground clearance. The cable specifications are given in Table 1.

Table 1. Necessary parameters to model the cable.

RADOX 155/RADOX Elastomer S (FHLR4GC13X)					
Layer	**Diameter**	**Resistivity**	**Relative Permeability (μ_r)**	**Permittivity (ε_r)**	**Insulator Loss Factor (tan δ)**
Copper	5.4 mm	1.7×10^{-8}	1	1	
RADOX 155	7 mm			2.8	0.01
SCREEN	7.8 mm	2.82×10^{-8}	1	1	
RADOX Elastomer S	9.3 mm			4.8	0.01

2.2. Motor Winding Modeling

The MCTL model is essential for motor winding modeling in high-frequency drive systems, particularly those using WBG semiconductors. These systems operate at much higher switching frequencies than traditional silicon-based systems, introducing high-frequency effects like non-uniform voltage distribution and transient overvoltages. The MCTL model addresses these by accurately representing the electromagnetic behavior of motor windings, accounting for parasitic components such as capacitances, inductances, and resistances. These parameters are critical for understanding voltage stresses on the windings, especially at higher frequencies, where traditional lumped-element models fall short.

Key parameters to extract in motor winding modeling with the MCTL approach include turn-to-turn capacitance, turn-to-ground capacitance, self-inductance, and mutual inductance [7,15,16]. These factors influence voltage distribution and current flow, especially during high-frequency switching transients. Accurately calculating these parameters allows for a precise evaluation of voltage stress across the stator windings, helping to predict failure points and optimize insulation design.

The step-by-step procedure for modeling motor windings with MCTL involves several stages. First, the geometry of the stator winding is defined based on the number of turns and their arrangement in the motor. For the Toyota Prius 2010, the PMSM features 48 stator slots, each containing 11 turns, the model presented in Figure 3 [20]. After the geometry is established, the next step is to calculate the parasitic elements using a FEM solver like COMSOL (in this study, COMSOL Multiphysics 6.1 is used).

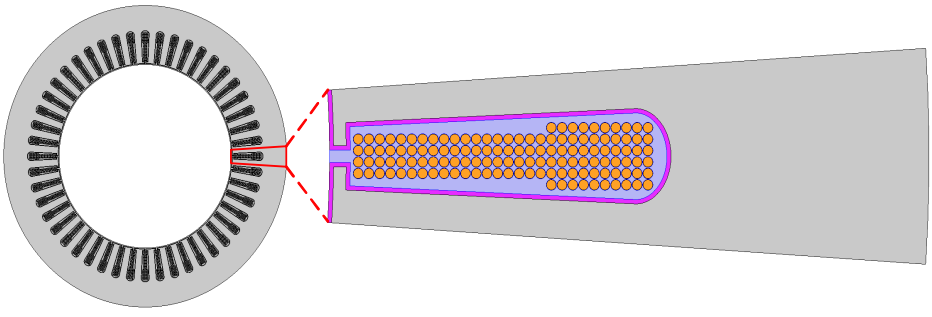

(**a**) (**b**)

Figure 3. FEM model implemented in COMSOL Multiphysics; (**a**) full stator model with 48 slots, (**b**) single-slot model.

For accurate field calculations, physics-controlled meshing with a finer element size is used in the electrostatics (es) and magnetic fields (mf) solvers to compute the inductance (L), resistance (R), and capacitance (C) of the motor winding system. This ensures that high-field gradient regions, such as conductor–insulator interfaces, are well-resolved. In electrostatics

(es), a finer mesh improves the accuracy of potential distributions, which is critical for capacitance estimation and dielectric behavior modeling. In mf, finer meshing around conductors captures effects like the skin and proximity effects, significantly influencing the frequency-dependent resistance and inductance calculations. These refinements ensure precise parameter extraction, particularly for high-frequency transient simulations.

2.2.1. Calculation of Turn Capacitance

Calculating turns' self- and mutual capacitance involves using an es solver. In this method, core boundaries are treated as ground, and one turn is excited with a nonzero voltage (e.g., 1 V), while others remain at 0 V. The process is repeated sequentially for all turns using a stationary source sweep to compute the capacitance matrix. This method does not require manual terminal voltage input as the software compensates for different voltage values.

The es solver works by solving Poisson's equation, which allows the calculation of Maxwell and mutual capacitance matrices. The equations are

$$\bigtriangledown \cdot \boldsymbol{D} = \rho_v \tag{13}$$

$$\boldsymbol{E} = -\bigtriangledown V \tag{14}$$

where $\boldsymbol{D}$ represents the electric displacement field, ρ_v represents volume charge, $\boldsymbol{E}$ electric field, and V represents the scalar potential field. Turn-to-core capacitance is calculated using a formula that accounts for both turn conductors, as presented in Equation (15).

$$C_{i0} = 2 \cdot \sum_{j=0}^{N_t} c_{ik} \tag{15}$$

where c_{ik} is the partial capacitance between turns i and k, and C_{i0} is the partial capacitance between turn i and the core. An additional factor 2 accounts for capacitance between the conductors of the turn and core. Turn-to-turn capacitance is computed by adjusting the mutual capacitance between turns using Equation (16).

$$C_{ik} = -c_{ik} \tag{16}$$

In the stator's overhang region, turn-to-core capacitance is neglected, and mutual capacitance is assumed to be equal to that of the slot region. This assumption, previously validated by experiments, is considered reliable for this study. So, the final capacitance is defined by Equation (17):

$$C_{ik} = -2c_{ik} \tag{17}$$

2.2.2. Calculation of Turn Inductance and Resistance

To calculate self and mutual inductances and resistances, the mf solver is used, where each turn is excited with a nonzero current (e.g., 1 A). In comparison, others are kept at 0 A. This process is repeated for all turns. The mf solver solves specific electromagnetic Equations (18)–(21) to compute these parameters.

$$\nabla \times \boldsymbol{H} = \boldsymbol{J} \tag{18}$$

$$\boldsymbol{B} = \nabla \times \boldsymbol{A} \tag{19}$$

$$\boldsymbol{J} = \sigma \boldsymbol{E} + j\omega \boldsymbol{D} + \sigma v \times \boldsymbol{B} + \boldsymbol{J_e} \tag{20}$$

$$\boldsymbol{E} = -j\omega \boldsymbol{A} \tag{21}$$

where the magnetic field is represented by $\boldsymbol{H}$, the electric current density is represented by $\boldsymbol{J}$, the magnetic flux density is represented by $\boldsymbol{B}$, the magnetic vector potential is represented by $\boldsymbol{A}$, σ represents the conductivity of the medium, the angular velocity is represented by ω, the electric displacement is measured by $\boldsymbol{D}$, and the electric field is represented by $\boldsymbol{E}$.

The inductances and resistances are evaluated at seven frequencies (50 Hz, 100 Hz, 1 kHz, 10 kHz, 100 kHz, 1 MHz, and 10 MHz) to capture frequency-dependent behaviors. The inductance and resistance are calculated using established formulas, such as Equations (22) and (23), from the stored magnetic energy and ohmic loss.

$$L = \frac{4U_{AV}}{I_p^2} \tag{22}$$

$$R = \frac{2P}{I_p^2} \tag{23}$$

A rational approximation approach called vector fitting models frequency-dependent inductances and resistances in the time domain. This method approximates the frequency-dependent function ($f(s)$) using a complex expression involving residues (c_n), poles (a_n), and coefficients (d, h) presented in Equation (24).

$$f(s) \approx \sum_{n=1}^{N} \frac{c_n}{s - a_n} + d + sh \tag{24}$$

Frequency-dependent self and mutual inductances and resistances are computed from the FEM simulation at the selected frequencies. These are represented as impedances in ladder circuits, approximated using vector fitting. The process of calculating the parameters precisely is discussed in detail in [15,16]. These results are then used to determine the components' frequency-dependent behavior, which is crucial for accurately representing the high-frequency effects in the windings.

The approach involves dividing the stator windings into smaller sections, called cells, and creating a detailed model for each cell that accounts for skin and proximity effects. By ensuring that each cell is sufficiently small, the model accurately predicts the voltage distribution across the stator windings, making the overall model a reliable representation of the motor windings. The minimum wavelength of a wave propagating in a transmission line is given by

$$\lambda = \frac{v}{f_{max}} \tag{25}$$

where v represents the wave propagation velocity, and f_{max} is the frequency up to which we need to model the circuit accurately. The wave propagation velocity is determined by the permittivity ε and permeability μ of the dielectric material and can be calculated using Equation (26):

$$v = \frac{1}{\sqrt{\mu\varepsilon}} \tag{26}$$

For the Toyota Prius 2010 motor, the relative permittivity of the insulation material is typically assumed to be 4.5, leading to a wave propagation velocity $v \approx 0.47 \times 3 \times 10^8$ m/s.

Given that the maximum frequency to consider is related to the rise time (t_r) of the switching pulse, the highest frequency f_{max} is defined as follows:

$$f_{max} = \frac{3}{\pi t_r} \tag{27}$$

For a rise time of 20 ns, the highest frequency to consider is approximately 5 MHz, ensuring that the model captures the relevant high-frequency effects without significant error.

Once the parameters are calculated using the FEM model simulation, using the flowchart shown in Figure 4, the vector fitting approximates the frequency-domain responses for the resistance and inductance value used in the ladder circuit shown in Figure 5 for the stator coil. This step converts the frequency-dependent parameters into time-domain equivalents for transient simulations. The resulting data are then represented using ladder circuits in the EMTP simulation tool, with each circuit element corresponding to a specific parasitic component in the motor winding.

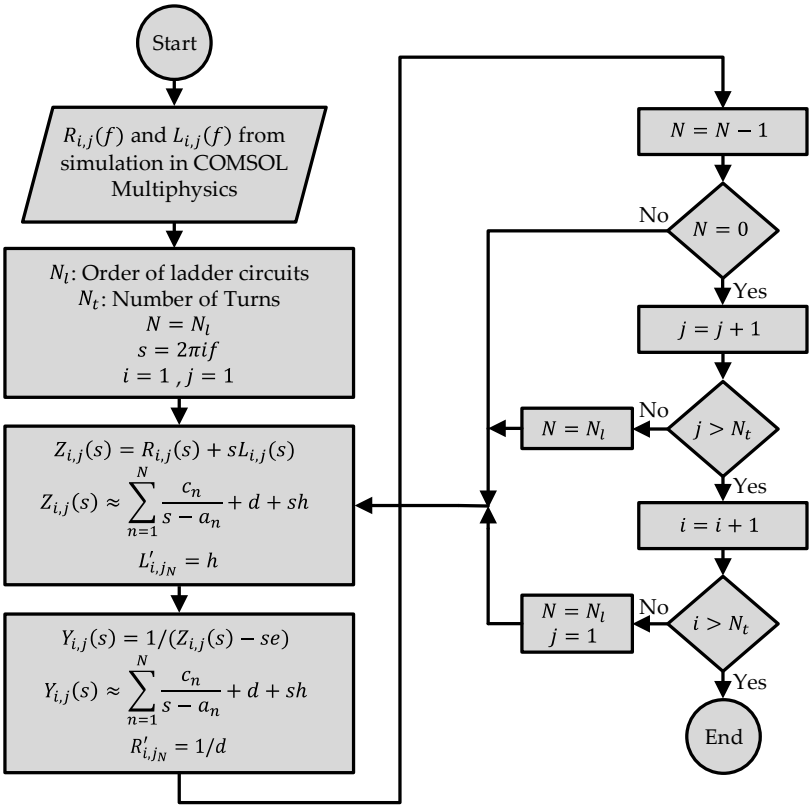

Figure 4. Flowchart to calculate the elements of ladder circuits using vector fitting.

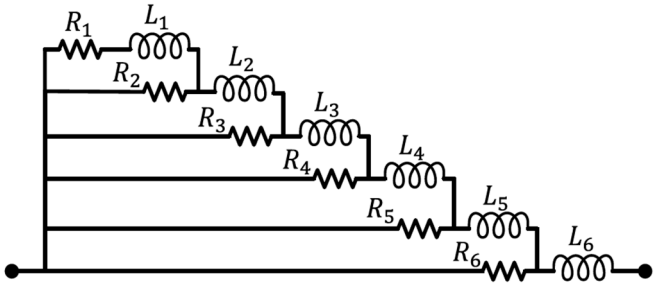

Figure 5. Six-layer ladder circuit-implemented in stator winding modeling [16].

The calculation process is described in detail in [16], and the motor details are described in Table 2 [20].

Table 2. Stator information of the PMSM employed in Toyota Prius 2010.

Stator Wiring		Lamination Parameters		Insulation	
Parameter	**Value**	**Parameter**	**Value**	**Parameter**	**Value**
Number of stator slot	48	Stator OD	26.4 cm	Thickness of wire insulation	0.025 mm
Stator turns per coil	11	Stator ID	16.19 cm	Thickness of ground wall insulation	0.35 mm
Parallel circuit per phase	0	Stator stack length	5.08 cm	The permittivity of turn insulation	3.5 $C^2/N{\cdot}m^2$
Coils in series per phase	8	Lamination thickness	0.305 mm	The permittivity of main wall insulation	3.5 $C^2/N{\cdot}m^2$
Number of wires parallel in each turn	12				
Wire size	20 AWG				
Phase resistance at 21 °C	0.077 Ω				
Slot depth	30.9 mm				
Slot opening	1.88 mm				

Finally, the turn model is implemented, where each turn of the motor winding is treated as an individual cell in the MCTL model using EMTP, as described in [16] and shown in Figure 6. The turn model includes self-resistance, self-inductances, and mutual resistance and inductances between turns. The mutual capacitances between turns are also considered, but only those significantly impacting the overall voltage distribution are included. The turn model allows for a detailed representation of voltage stresses, particularly in the first few turns closest to the motor terminals, where the highest voltage gradients are typically observed.

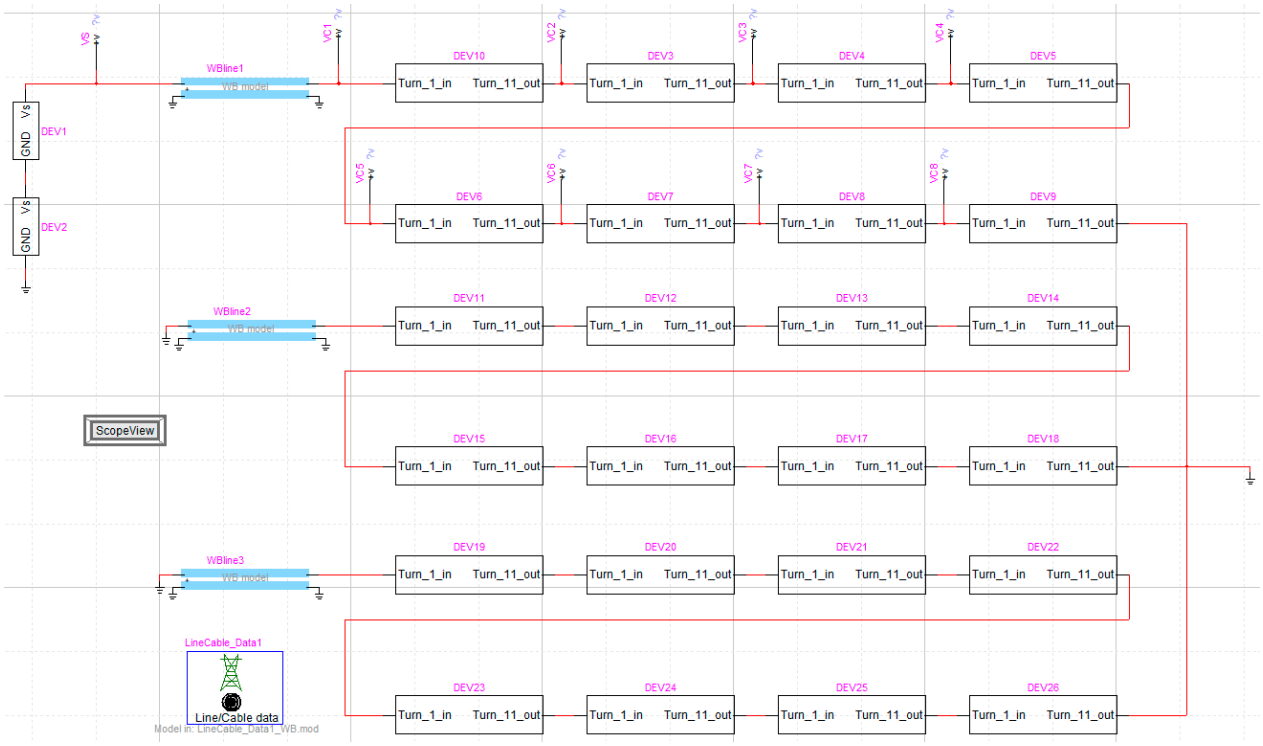

Figure 6. Three-phase neutral grounded EMTP-RV model of PMSM.

3. Results and Discussion

After completing the MCTL modeling of the motor stator and the WB and CP modeling of the cable, different scenarios need to be simulated, and the results will be discussed. It is widely accepted that the motor winding turns closer to the motor terminals face larger voltages than other turns, but the result may differ due to the ground connection at the neutral point. In our case, we will observe the response of both single and three-phase simulations of the motor winding using the CP and WB models in the cable.

3.1. One-Phase Simulation

A one-phase stator windings model is implemented and connected to the inverter model through a 36-inch predefined cable. The inverter is fed from a 560 V DC link and generates 100 kHz PWM voltages with t_r = 20 ns. Note that a 36-inch cable is used to ensure a case close to the considered Toyota Prius 2010. Figure 7 shows the schematic circuit diagram we have considered in our simulation. We considered two cases: one is the floating neutral point of the motor winding, and another one is the grounded neutral point of the motor winding. In the figures, we have mentioned all three phases of the PMSM's winding and the connected cable, which will eventually carry the voltage wave from the inverter. For this simulation scenario, each phase is connected to the cable of the mentioned length. The cable is connected to the voltage source. During the one-phase simulation, we disregarded the circuit's Phase B and Phase C portions along with its connecting cable. That means we have only considered the source, the cable associated with Phase A, and the winding of Phase A. We have considered the CP model and WB model of the connecting cable in different simulation scenarios.

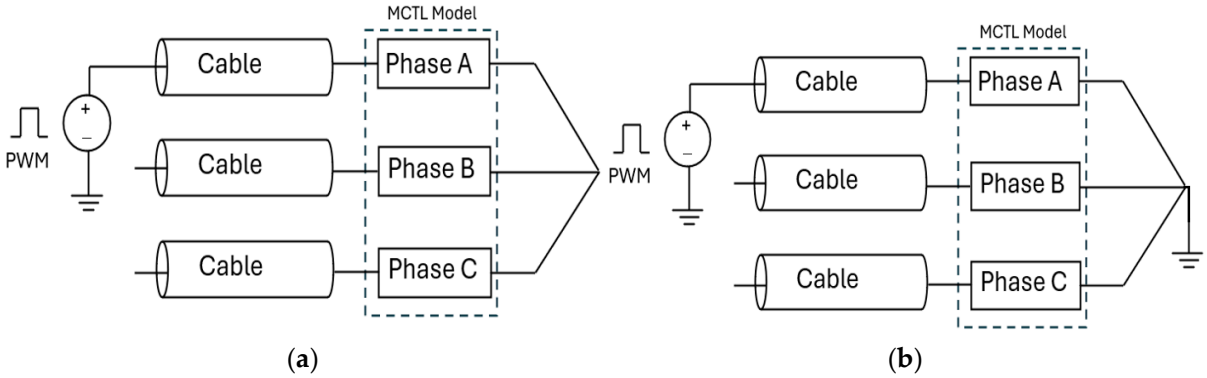

Figure 7. Three phase modeling: (**a**) floating neutral point and (**b**) neutral grounded.

Figures 8–10 show the effect of the CP and WB modeling of the cable while only a single phase is considered and the neutral point is not grounded. The difference between the two models is that the CP model estimates more harmonics than the WB model in this case, though the amplitude of the transient voltage is the same. Figures 8–10 show that the first coil, which is nearer to the cable, has a peak earlier than the other coils, but the other coil's peak is higher due to the charge accumulation on those lines' lack of grounding. Both figures show the same magnitude in each coil. Figure 10 shows the voltage of the first coil in both cases and clearly shows that the CP model estimates some harmonics that are not present in the WB model.

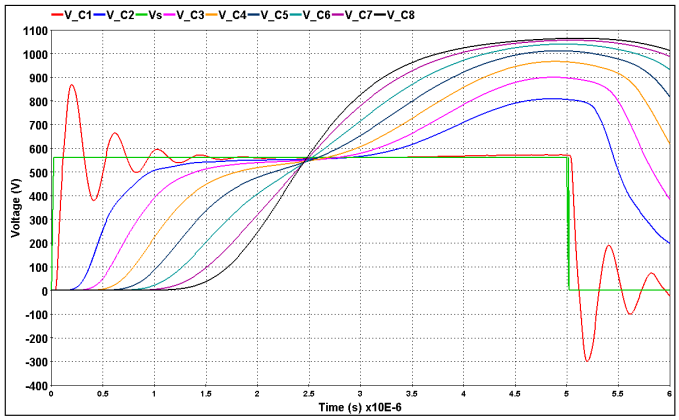

Figure 8. Coil-to-core voltages when a single-phase model is implemented with WB cable modeling and is excited by 560 V PWM voltage with t_r = 20 ns and the neutral point floating.

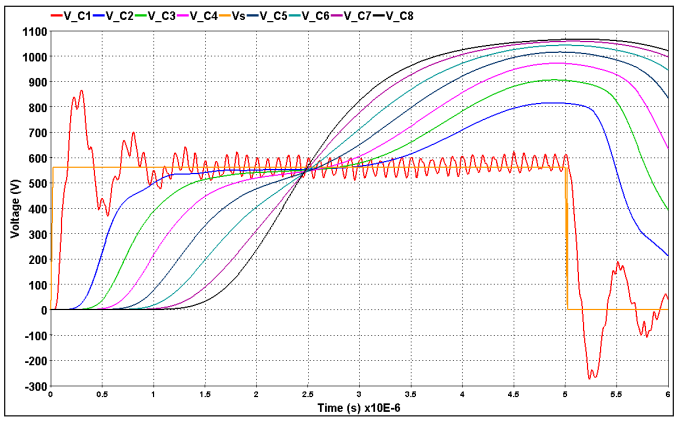

Figure 9. Coil-to-core voltages when a single-phase model is implemented with CP cable modeling and is excited by 560 V PWM voltage with t_r = 20 ns and the neutral point floating.

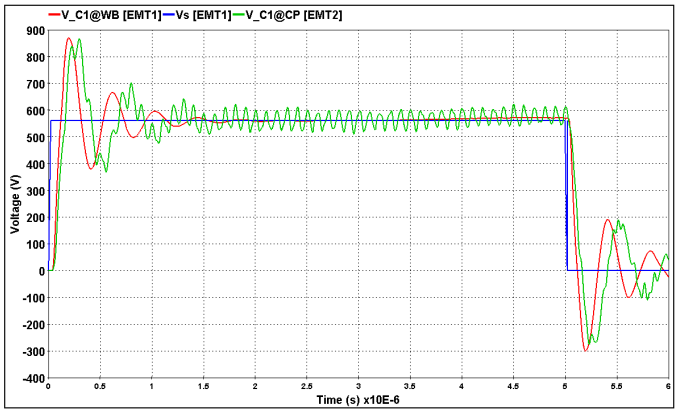

Figure 10. Coil-to-core voltages comparison of the first coil when a three-phase model is implemented with both CP and WB models and is excited by 560 V PWM voltage with t_r = 20 ns and the neutral point floating.

3.2. Three-Phase Simulation

In this part of the paper, we have considered three phases of the PMSM, but only one phase is exciting using a 560 V PWM signal like the schematic diagram shown in Figure 7. Figures 11–13 show the effect of the CP and WB modeling of the cable while only a single phase is exciting among the three phases and the neutral point is not grounded. The difference between the two models is that, like the previous case, the CP model estimates some harmonics compared to the WB model, and the amplitude of the transient voltage is

predicted higher by the CP. Figures 11 and 12 show that the first coil, nearer to the motor terminal, has a peak earlier than the other coils and is higher than the other coils' peak. Both figures show the same magnitude except for the first coil. Figure 13 shows the voltage of the first coil in both cases and clearly shows that the CP model estimates some harmonics that are not present in the WB model. A significant concern is that the CP model shows peak voltage magnitude at about 1 kV, but the WB model imitates it as 760 V.

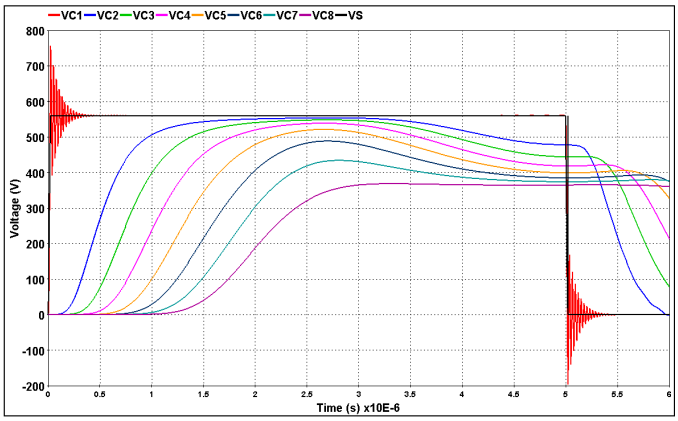

Figure 11. Coil-to-core voltages when a three-phase model is implemented using the WB model for cable and is excited by 560 V PWM voltage with t_r = 20 ns and the neutral point floating.

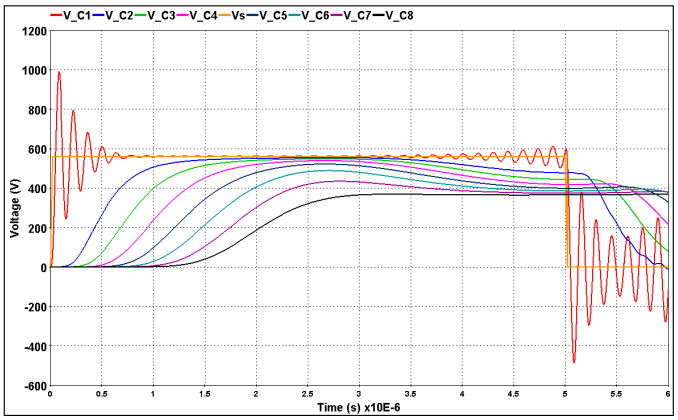

Figure 12. Coil-to-core voltages when a three-phase model is implemented using the CP model for cable and is excited by 560 V PWM voltage with t_r = 20 ns and the neutral point floating.

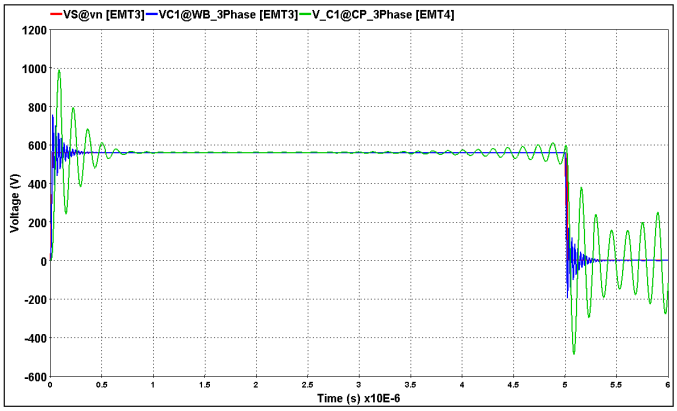

Figure 13. Coil-to-core voltage comparison of the first coil when a three-phase model is implemented using both CP and WB models and is excited by 560 V PWM voltage with t_r = 20 ns and the neutral point floating.

To evaluate the impact of grounding on transient behavior, simulations were conducted with both floating and grounded neutral configurations (Figure 7). The choice of grounding may influence how transient voltages propagate across motor windings. In the floating neutral case, the absence of a low-impedance return path results in higher common-mode voltage levels, increasing the likelihood of capacitive coupling effects and differential overvoltages. Conversely, grounding the neutral point provides a controlled return path, reducing common-mode voltage buildup and improving transient stability. However, this configuration may also introduce circulating currents, which must be considered in insulation design and transient suppression strategies.

In this part of the study, we considered a three-phase PMSM with a grounded neutral where only one phase was excited using a 560 V PWM signal, as depicted in Figure 7. Figures 14–16 illustrate the effect of CP and WB cable modeling under this configuration. Similar to previous cases, the CP model predicts more harmonics than the WB model, though both models estimate similar transient voltage amplitudes. Figures 14 and 15 show that the first coil closest to the motor terminal reaches its peak voltage earlier than the other coils and exhibits the highest peak magnitude. Both figures show nearly identical magnitudes across the coils, except for the first one.

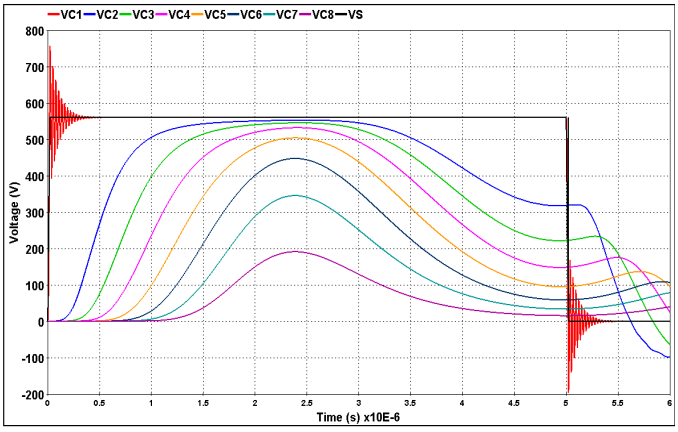

Figure 14. Coil-to-core voltages when a three-phase model is implemented using the WB model for cable and excited by a 560 V PWM voltage with t_r = 20 ns and the neutral point grounded.

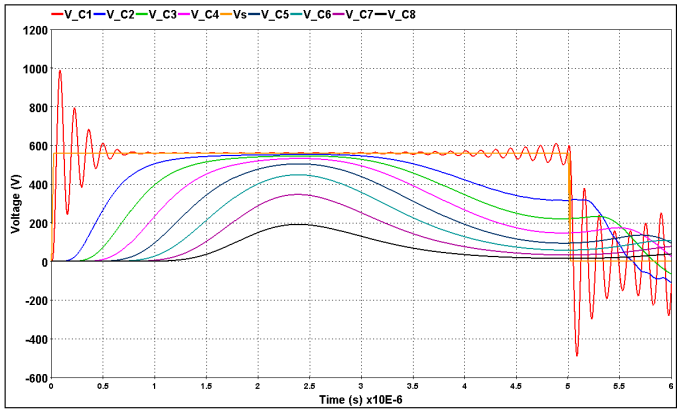

Figure 15. Coil-to-core voltages when a three-phase model is implemented using the CP model for cable, excited by a 560 V PWM voltage with t_r = 20 ns and the neutral point grounded.

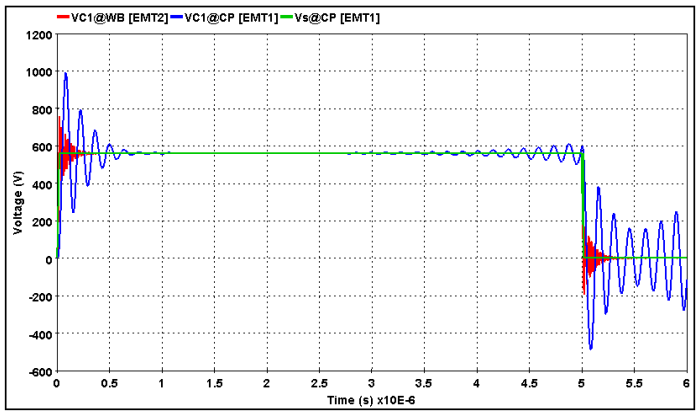

Figure 16. Coil-to-core voltages comparison of the first coil when a three-phase model is implemented, excited by a 560 V PWM voltage with t_r = 20 ns and the neutral point grounded.

Figure 16 highlights the voltage behavior of the first coil for both CP and WB models. The CP model overestimates specific harmonics not observed in the WB model. Additionally, the transient voltage in the CP model takes longer to stabilize, whereas the WB model more accurately captures the damping effects, resulting in quicker voltage stabilization. Another significant observation is that the CP model predicts a peak voltage magnitude of approximately 1 kV. In contrast, the WB model provides a more realistic estimation of 760 V.

The figures above demonstrate that the CP and WB models exhibit similar behaviors, except for the first coil. In both cases, the CP model shows that the transient voltage in the first coil takes longer to stabilize. However, with its more accurate cable modeling, the WB model achieves much faster voltage stabilization. This behavior is further clarified by the Fourier analysis of the first coil's voltage, shown in Figure 17. The WB and CP models contain higher frequency components during the transient analysis. However, the CP model has higher magnitude and lower frequency components than the WB model. This results in the WB model providing a more realistic transient response. The higher magnitude of the lower frequency components in the CP model amplifies peak values during the transient analysis as they interact with the fundamental frequency.

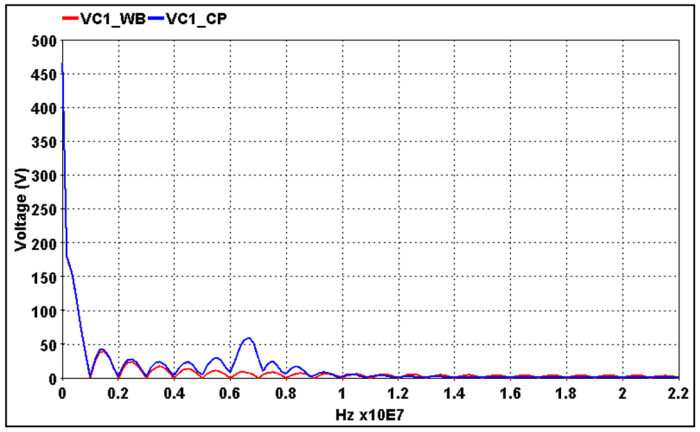

Figure 17. Fourier analysis of the transient voltage generated in the first coil using the WB and CP models.

Various techniques have been developed to mitigate these transient overvoltages at motor terminals. Passive dv/dt filters utilize a band-stop R-L-C circuit, where the resistor provides damping and impedance matching. In contrast, the LC circuit suppresses reflected wave oscillations, offering a low-loss, compact alternative to active filters [25]. A

regenerative inverter output dv/dt filter replaces the passive resistor in an LCR filter with a GaN-based full-bridge converter, recycling filter path energy and reducing filter size while enhancing efficiency [26]. Active dv/dt filtering with FPGA control precisely regulates inverter switching signals to control voltage rise time, achieving effective overvoltage suppression with a smaller passive filter [27]. Lastly, the parallel inverter topology connects multiple inverters directly to the motor terminals, balancing current and reducing transient overvoltages without additional passive filtering [28]. These techniques provide diverse solutions to minimize insulation stress and improve motor drive system reliability.

4. Conclusions

This study presents a comprehensive approach to modeling and analyzing transient overvoltage phenomena in EV powertrains, focusing on WB cable modeling and MCTL motor winding analysis. Our findings show that the WB model, implemented in EMTP-RV, more accurately captures high-frequency transient effects—such as voltage reflections and oscillations—than the conventional CP model. Similarly, the MCTL approach provides deeper insights into non-uniform voltage distributions in motor windings, emphasizing the importance of precisely modeling parasitic elements like capacitances, inductances, and resistances.

Using COMSOL Multiphysics for parasitic element calculations and vector fitting for frequency-domain approximation for designing the motor winding, we identified key voltage stress hotspots, particularly in the turns closest to motor terminals. Incorporating real-world data from a Toyota Prius 2010 model confirmed the accuracy and reliability of our proposed models, reinforcing their practical applicability for EV systems. These insights can help optimize cable and motor designs, ultimately improving the durability and efficiency of WBG inverter-driven EV powertrains.

Beyond EVs, these findings can be extended to other vehicle types, including hybrid and fully electric commercial vehicles, where transient overvoltage effects significantly impact insulation system design. This work offers valuable guidance for improving insulation strategies in electric buses, trucks, and next-generation high-performance EVs.

For future research, integrating these models with advanced insulation materials, such as nanocomposite dielectrics or high-temperature polyimides, could enhance system reliability and longevity. Extending the analysis to heavy-duty electric trucks, electric aircraft, and marine applications would provide a broader perspective on the evolving challenges in high-voltage powertrain design. Exploring mitigation techniques like optimized winding layouts, shielding strategies, and active transient suppression circuits could improve insulation performance and overall system efficiency.

Author Contributions: Conceptualization, E.A. and M.G.; methodology, E.A. and M.G.; software, E.A. and M.G.; validation, E.A. and M.G.; formal analysis, E.A. and M.G.; investigation, E.A. and M.G.; resources, E.A. and M.G.; data curation, E.A. and M.G.; writing—original draft preparation, E.A.; writing—review and editing, M.G.; visualization, E.A. and M.G.; supervision, M.G.; project administration, M.G.; funding acquisition, M.G. All authors have read and agreed to the published version of the manuscript.

Funding: This work was partly supported by the National Science Foundation (NSF) under Award 2306093.

Data Availability Statement: Data are contained within the article.

Conflicts of Interest: The authors declare no conflicts of interest.

References

1. Rafin, S.M.S.H.; Ahmed, R.; Mohammed, O.A. Wide Band Gap Semiconductor Devices for Power Electronic Converters. In Proceedings of the 2023 Fourth International Symposium on 3D Power Electronics Integration and Manufacturing (3D-PEIM), Miami, FL, USA, 1–3 February 2023; pp. 1–8.
2. Husain, I.; Ozpineci, B.; Islam, M.S.; Gurpinar, E.; Su, G.-J.; Yu, W.; Chowdhury, S.; Xue, L.; Rahman, D.; Sahu, R. Electric Drive Technology Trends, Challenges, and Opportunities for Future Electric Vehicles. *Proc. IEEE* **2021**, *109*, 1039–1059. [CrossRef]
3. Morya, A.K.; Gardner, M.C.; Anvari, B.; Liu, L.; Yepes, A.G.; Doval-Gandoy, J.; Toliyat, H.A. Wide Bandgap Devices in AC Electric Drives: Opportunities and Challenges. *IEEE Trans. Transp. Electrif.* **2019**, *5*, 3–20. [CrossRef]
4. Woo, K.; Bian, Z.; Noshin, M.; Martinez, R.P.; Malakoutian, M.; Shankar, B.; Chowdhury, S. From Wide to Ultrawide-Bandgap Semiconductors for High Power and High Frequency Electronic Devices. *J. Phys. Mater.* **2024**, *7*, 022003. [CrossRef]
5. Li, S.; Lu, S.; Mi, C.C. Revolution of Electric Vehicle Charging Technologies Accelerated by Wide Bandgap Devices. *Proc. IEEE* **2021**, *109*, 985–1003. [CrossRef]
6. Ghassemi, M. Accelerated Insulation Aging Due to Fast, Repetitive Voltages: A Review Identifying Challenges and Future Research Needs. *IEEE Trans. Dielectr. Electr. Insul.* **2019**, *26*, 1558–1568. [CrossRef]
7. Cortes, F.P.E.; Gomez, P.; Hussain, M.K. Modeling and Simulation of Rotating Machine Windings Fed by High-Power Frequency Converters for Insulation Design. In *Simulation and Modelling of Electrical Insulation Weaknesses in Electrical*; IntechOpen: London, UK, 2018. [CrossRef]
8. Saha, A.; Ghassemi, M. A Review of Electrical Insulation Challenges for Electrical Powertrain Components in the Future More and All Electric Aircraft under Low-Pressure Conditions. *IEEE J. Emerg. Sel. Topics Power Electron.* 2024; *in press*. [CrossRef]
9. Zhang, B.; Jiang, X.; Li, K.; Yang, Z.; Li, X.; Chang, G.; Ghassemi, M. Dielectric Properties Characterization and Evaluation of Commercial Silicone Gels for High-Voltage High-Power Power Electronics Module Packaging. *IEEE Trans. Dielectr. Electr. Insul.* **2023**, *30*, 210–219. [CrossRef]
10. Bilal, G.; Gomez, P.; Salcedo, R.; Villanueva-Ramirez, J.M. Electromagnetic Transient Studies of Large Distribution Systems Using Frequency Domain Modeling Methods and Network Reduction Techniques. *Int. J. Electr. Power Energy Syst.* **2019**, *110*, 11–20. [CrossRef]
11. Ramos-Leanos, O.; Naredo, J.L.; Mahseredjian, J.; Dufour, C.; Gutierrez-Robles, J.A.; Kocar, I. A Wideband Line/Cable Model for Real-Time Simulations of Power System Transients. *IEEE Trans. Power Del.* **2012**, *27*, 2211–2218. [CrossRef]
12. Clayton, R.P. *Analysis of Multiconductor Transmission Lines*; Wiley-IEEE Press: Hoboken, NJ, USA, 2008.
13. McLaren, P.G.; Oraee, H. Multiconductor Transmission-Line Model for the Line-End Coil of Large AC Machines. *IEE Proc. B Electr. Power Appl.* **1985**, *132*, 149–156. [CrossRef]
14. Guardado, J.L.; Cornick, K.J. A Computer Model for Calculating Steep-Fronted Surge Distribution in Machine Windings. *IEEE Trans. Energy Convers.* **1989**, *4*, 95–101. [CrossRef]
15. Sundeep, S.; Wang, J.; Griffo, A. Holistic Modeling of High-Frequency Behavior of Inverter-Fed Machine Winding, Considering Mutual Couplings in Time Domain. *IEEE Trans. Ind. Appl.* **2021**, *57*, 6044–6057. [CrossRef]
16. Barzkar, A.; Ghassemi, M. Precise Evaluation of Repetitive Transient Overvoltages in Motor Windings in Wide-Bandgap Drive Systems. *Vehicles* **2022**, *4*, 697–726. [CrossRef]
17. Liu, B.; Wu, X.; Leary, A.; Choksi, K.; Wu, Y.; Luo, F. Modeling and Mitigation of dv/dt and Transmission Line Effect for Motor Drive System in Electric Aircraft Propulsion. In Proceedings of the IEEE Energy Conversion Congress and Exposition (ECCE), Nashville, TN, USA, 29 October–2 November 2023; pp. 5206–5212. [CrossRef]
18. Peng, H.; Yu, Y.; Hameyer, K. Conductor-Based Modeling of a Single-Tooth Winding for EMI Simulation. *IEEE Trans. Power Electron.* **2024**, *39*, 11099–11109. [CrossRef]
19. Hewitt, D.A.; Sundeep, S.; Wang, J.; Griffo, A. High Frequency Modeling of Electric Machines Using Finite Element Analysis Derived Data. *IEEE Trans. Ind. Electron.* **2024**, *71*, 1432–1442. [CrossRef]
20. Burress, T.A.; Campbell, S.L.; Coomer, C.; Ayers, C.W.; Wereszczak, A.A.; Cunningham, J.P.; Marlino, L.D.; Seiber, L.E.; Lin, H.-T. *Evaluation of the 2010 Toyota Prius Hybrid Synergy Drive System*; Oak Ridge National Lab. (ORNL), Power Electronics and Electric Machinery Research Facility: Oak Ridge, TN, USA, 2011.
21. Bewley, L.V. Traveling Waves on Transmission Systems. *Trans. Am. Inst. Electr. Eng.* **1931**, *50*, 532–550. [CrossRef]
22. Magalhães Júnior, F.M.; Lopes, F.V. Mathematical Study on Traveling Waves Phenomena on Three Phase Transmission Lines –Part II: Reflection and Refraction Matrices. *IEEE Trans. Power Deliv.* **2022**, *37*, 1161–1170. [CrossRef]
23. Martinez-Velasco, J.A. *Power System Transients: Parameter Determination*; CRC Press: Boca Raton, FL, USA, 2017; ISBN 978-1-4200-6530-5.
24. HUBER+SUHNER. RADOX Elastomer S (FHLR91XC13X and FHLR4GC13X). Available online: https://www.hubersuhner.com/en/shop/product/cables/power-cables/84132059/radox-elastomer-s-fhlr91xc13x-and-fhlr4gc13x (accessed on 20 December 2024).
25. Wang, N.; Wang, Z.; Liu, Z.; Xin, G.; Shi, X.; Kang, Y. A Band-Stop-Type dv/dt Filter for Terminal Overvoltage Mitigation of SiC Motor Drives. *IEEE Trans. Power Electron.* **2024**, *39*, 16391–16399. [CrossRef]

26. Haque, M.E.; Sozer, Y.; Siddiquee, A. Regenerative dV/dt Filter Topology for Motor Drives. In Proceedings of the 2024 IEEE Applied Power Electronics Conference and Exposition (APEC), Long Beach, CA, USA, 25–29 February 2024; pp. 2377–2384. [CrossRef]
27. Korhonen, J.; Ström, J.-P.; Tyster, J.; Silventoinen, P.; Sarén, H.; Rauma, K. Control of an Inverter Output Active du/dt Filtering Method. In Proceedings of the 35th Annual Conference of IEEE Industrial Electronics (IECON 2009), Porto, Portugal, 3–5 November 2009; pp. 316–321. [CrossRef]
28. Korhonen, J.; Itkonen, T.; Ström, J.-P.; Tyster, J.; Silventoinen, P.T. Active Motor Terminal Overvoltage Mitigation Method for Parallel Voltage Source Inverters. *IET Power Electron.* **2012**, *5*, 1023–1031. [CrossRef]

Disclaimer/Publisher's Note: The statements, opinions and data contained in all publications are solely those of the individual author(s) and contributor(s) and not of MDPI and/or the editor(s). MDPI and/or the editor(s) disclaim responsibility for any injury to people or property resulting from any ideas, methods, instructions or products referred to in the content.